J. Fluid Mech. (2002), *vol.* 455, *pp.* 289–314.
DOI: 10.1017/S0022112001007431 Printed in the United Kingdom

The instability and breakdown of a near-wall low-speed streak

By MASAHITO ASAI[1], MASAYUKI MINAGAWA[1] AND MICHIO NISHIOKA[2]

[1]Department of Aerospace Engineering, Tokyo Metropolitan Institute of Technology, Asahigaoka 6-6, Hino, Tokyo 191-0065, Japan

[2]Department of Aerospace Engineering, Osaka Prefecture University, Gakuencho 1-1, Sakai, Osaka 599-8531, Japan

(Received 17 April 2000 and in revised form 27 September 2001)

The instability of the three-dimensional high-shear layer associated with a near-wall low-speed streak is investigated experimentally. A single low-speed streak, not unlike the near-wall low-speed streaks in transitional and turbulent flows, is produced in a laminar boundary layer by using a small piece of screen set normal to the wall. In order to excite symmetric and anti-symmetric modes separately, well-controlled external disturbances are introduced into the laminar low-speed streak through small holes drilled behind the screen. The growth of the excited symmetric varicose mode is essentially governed by the Kelvin–Helmholtz instability of the inflectional velocity profiles across the streak in the normal-to-wall direction and it can occur when the streak width is larger than the shear-layer thickness. The spatial growth rate of the symmetric mode is very sensitive to the streak width and is rapidly reduced as the velocity defect decreases owing to the momentum transfer by viscous stresses. By contrast, the anti-symmetric sinuous mode that causes the streak meandering is dominated by the wake-type instability of spanwise velocity distributions across the streak. As far as the linear instability is concerned, the growth rate of the anti-symmetric mode is not so strongly affected by the decrease in the streak width, and its exponential growth may continue further downstream than that of the symmetric mode. As for the mode competition, it is important to note that when the streak width is narrow and comparable with the shear-layer thickness, the low-speed streak becomes more unstable to the anti-symmetric modes than to the symmetric modes. It is clearly demonstrated that the growth of the symmetric mode leads to the formation of hairpin vortices with a pair of counter-rotating streamwise vortices, while the anti-symmetric mode evolves into a train of quasi-streamwise vortices with vorticity of alternate sign.

1. Introduction

The present experimental study is conducted to shed some light on the dynamics of near-wall turbulence, in particular on the mechanism by which near-wall coherent structures are generated and sustained. Since the experimental studies on the laminar to turbulent transition of plane Poiseuille flow (Nishioka, Iida & Ichikawa 1975; Nishioka, Asai & Iida 1980), we have been working on the problem of transition to wall turbulence with an insight that turbulence is caused and then sustained by a sequence of flow instabilities. Today, we all know that the occurrence of low-speed

streaks and the associated generation of hairpin vortices and/or quasi-streamwise vortices are the phenomena dominating the near-wall turbulence. From an instability point of view, the cited near-wall activities occur in a quasi-periodic manner and are only significant where the momentum thickness Reynolds number is above a certain threshold. It is also to be stressed that the low-speed streaks are always surrounded by high-shear regions. This is, of course, the case for a single low-speed streak too. In other words, inflectional velocity distributions appear across a low-speed streak in the spanwise direction as well as in the normal-to-wall direction. Without strong viscous effects, the inflectional velocity field is expected to be highly unstable even though it is three-dimensional. It is therefore very important to realize the streak instability in this sense under well-controlled flow conditions and thus to examine whether the streak instability can operate as a dominant mechanism for generating and sustaining coherent structures such as high-speed and low-speed streaks, quasi-streamwise vortices and hairpin vortices. With these motivations in mind, an experimental study is conducted on the instability of a single low-speed streak in a laminar boundary layer. Before describing the experiment, a brief review of previous studies on related subjects is in order.

The near-wall streaky structure with high- and low-speed regions aligned in the streamwise direction was first visualized in the developed turbulent boundary layer by Kline *et al.* (1967). They suggested that the near-wall low-speed streaks with an average spanwise spacing of about 100 wall units play an important role in generating the turbulent energy through a sequence of bursting events. The appearance of low-speed streaks and a near-wall activity similar to bursting were also observed in the final stages of laminar–turbulent transition initially controlled by the convective growth of Tollmien–Schlichting waves. In the so-called ribbon-induced transition where periodic Tollmien–Schlichting waves are introduced by means of a vibrating ribbon, the phenomenon of wall turbulence generation occurs in the late stage of high-frequency secondary instability, i.e. the breakdown of thin internal shear layers (formed away from the wall) into high-frequency hairpin vortices. Through a series of ribbon-induced transition experiments of plane Poiseuille flow, Nishioka, Asai & Iida (1981) and Nishioka & Asai (1984) were the first to show this near-wall phenomenon similar to a bursting event. That is, after the passage of hairpin vortices resulting from the high-frequency secondary instability, near-wall fluid is lifted up to develop a low-speed streak in between neighbouring high-speed regions. The uplifted wall shear layer along the low-speed region soon then evolves (or breaks down) into near-wall vortices. Through numerical simulations, Sandham & Kleiser (1992) and Rist & Fasel (1995) later reproduced the disturbance development observed in the ribbon-induced transition experiments. In these transition studies, hairpin vortices were identified as the key elements directly triggering the occurrence of wall turbulence structure, though the details of the near-wall bursting events were not sufficiently clarified. In order to do so, Asai & Nishioka (1990, 1995*a*, *b*) and Nishioka, Asai & Furumoto (1994) further examined the occurrence of wall turbulence structure through the observation of a subcritical boundary-layer transition triggered by hairpin vortices. Their experiments showed that near-wall low-speed streaks developing after the passage of primary (initially excited) hairpin vortices were lifted up into a succession of hairpin-like vortices (usually not symmetric but asymmetric with one dominant streamwise vortex) for momentum thickness Reynolds numbers above 130. The intensity of the primary hairpin vortices capable of triggering the subcritical transition was found to be of the order of 10% of the free-stream velocity in terms of the r.m.s. value of u-fluctuations and about 5% of the free-stream velocity in terms of the magnitude of instantaneous

v-fluctuations. The existence of a critical condition for the successive occurrence of hairpin vortices strongly suggests the instability of near-wall flow with low-speed streaks.

In the lateral growth of turbulent spots or turbulent wedges, low-speed streaks appear in succession in the ambient laminar flow region on both sides of the spot or wedge, as visualized, for instance, by Mochizuki (1961), Matsui (1980), Perry, Lim & Teh (1981), Carlson, Widnall & Peeters (1982), Acarlar & Smith (1987*a*, *b*), Haidari & Smith (1994), Asai, Sawada & Nishioka (1996), and Asai & Nishioka (1997). As far as these low-Reynolds-number visualization studies are concerned, hairpin-like vortices are generated from near-wall low-speed streaks through their breakdown. Note that the low-speed streak appearing on each side of the turbulent wedge is initially accompanied by a streamwise vortex, which, through the interaction with the wall, soon induces a secondary vortex with vorticity of opposite sign and then a pair of counter-rotating vortices: see Doligalski, Smith & Walker (1994). The occurrence of low-speed streaks for the case of the development of a single hairpin vortex was examined experimentally by Smith *et al.* (1991) and Haidari & Smith (1994) and numerically by Singer & Joslin (1994) and Zhou *et al.* (1999). According to their results, low-speed streaks appear outsides hairpin legs, in addition to the primary low-speed streaks along each hairpin leg and between both legs. The latter feature was explained by vortex-induced unsteady separation as analysed theoretically by Van Dommelen & Cowley (1990) and Peridier, Smith & Walker (1991*a*, *b*). The breakdown of these low-speed streaks leading to the regeneration of hairpin vortices is also associated with the inflectional instability of low-speed streaks.

In developed wall turbulence, on the other hand, on the basis of the results of direct numerical simulations (DNS), Robinson (1991) identified asymmetric hairpin (or horseshoe) vortices and quasi-streamwise vortices as two dominant coherent vortices in wall turbulence, quasi-streamwise vortices close to the wall and hairpin vortices in the log-law region. Johansson, Alfredsson & Kim (1991) analysed the DNS data of turbulent channel flow and showed the importance of asymmetry of near-wall streaky structures. Jimenez & Moin (1991) also demonstrated through the DNS of a so-called minimal flow unit that a single inclined quasi-streamwise vortex was a dominant structure in the near-wall region. To identify the coherent vortices in wall turbulence more accurately, Jeong & Hussain (1995) proposed a vortex identification technique based on local pressure minima induced by vortices. Jeong *et al.* (1997) analysed the DNS data of Kim, Moin & Moser (1987) by using such a detection technique, and identified the typical quasi-streamwise vortices associated with the near-wall low-speed streaks. Also see Schoppa & Hussain (1997, 2000). Through the direct numerical simulation of a minimal plane Couette flow unit with streamwise and spanwise periodic boundary conditions at the lowest critical Reynolds number for sustaining wall turbulence, Hamilton, Kim & Waleffe (1995) proposed a regeneration mechanism of such near-wall streamwise vortices and associated low-speed streaks. In the regeneration cycle they proposed, the occurrence of near-wall streamwise vortices results from a sinuous mode instability of low-speed streaks leading to the meandering wavy motion of the streaks. Itano & Toh (2001) also found a similar travelling-wave solution corresponding to the nonlinear saturation stage of the streak instability for a minimal channel flow.

Streak instability is also considered to govern the secondary instability process occurring beyond the growth of Görtler vortices on a concave wall. In Görtler flows, as observed by Swearingen & Blackwelder (1987), low-speed streaks caused by each pair of counter-rotating streamwise vortices undergo a secondary instability to

generate hairpin-shaped (or arch-like) vortices or wavy meandering motions of Görtler vortices. Also see the review by Saric (1994). The secondary instability is no doubt caused by the associated inflectional velocity profiles both in the normal-to-wall and spanwise directions, which can excite both varicose and sinuous instability modes. Hall & Horseman (1991), Yu & Liu (1991) and Park & Huerre (1994) studied theoretically the mechanism of the secondary inflectional instability of Görtler vortices leading to the development of sinuous and varicose modes on the basis of three-dimensional stability equations. Similar instability phenomena have been observed in by-pass boundary-layer transition caused by high-intensity free-stream turbulence (Morkovin & Reshotko 1990). The by-pass transition results from the algebraic growth of non-modal disturbances known as transient growth since Landahl (1980) and Hultgren & Gustavsson (1981). Through solving an optimization problem for the development of low-speed streaks under specific constraints on the initial conditions for disturbances involving cross-stream velocity perturbations, Andersson, Berggren & Henningson (1999) and Luchini (2000) proposed that stationary or low-frequency streamwise streaks with a preferable spanwise wavelength about eight times the displacement thickness of the laminar boundary layer undergo the maximum spatial transient growth. Matsubara *et al.* (2000) demonstrated experimentally that the growth of near-wall streaks is a key phenomenon triggering the by-pass transition and that when the near-wall streaks are intensified, a secondary instability occurs, which leads to a time-dependent oscillation of the streaks and subsequent breakdown into young turbulent spots. The related experiments by Westin *et al.* (1998) and Bakchinov *et al.* (1998) suggest that the occurrence of the secondary instability of streaks requires a rather large amplitude of velocity variation across the streaks. Elofsson, Kawakami & Alfredsson (1999) examined the growth and breakdown of near-wall streaks in plane Poiseuille flow at subcritical Reynolds numbers, and reported that the secondary instability leading to streak breakdown occurred when the streak amplitude (the velocity difference between high- and low-speed regions) exceeded a high threshold, for example, about 70% of the centre plane velocity at a Reynolds number of 2000.

Thus, the streak instability appears under various conditions in transitional and turbulent flows. As already stated, in order to examine if and how the streak instability can operate as a dominant mechanism for generating and sustaining coherent structures, it is important to realize the streak instability under well-controlled flow conditions. In the present experimental study, a single low-speed streak is produced in a laminar boundary layer by setting a small piece of screen (a wire-gauze) normal to the wall, and well-controlled artificial disturbances are introduced through small holes immediately behind the screen.

2. Experimental set-up and procedure

The whole experiment is conducted in a low-turbulence wind tunnel of open jet type. The wind tunnel has three damping screens spanning the diffuser and five damping screens and a honeycomb in the settling chamber of $1200 \times 1200\,\mathrm{mm}^2$ in cross-section. The area ratio of the contraction to the test section of $400 \times 400\,\mathrm{mm}^2$ is 9. As illustrated in figure 1, a boundary-layer plate, which is 10 mm thick and 1100 mm long, is set parallel to the oncoming uniform flow in the test section. The boundary-layer plate has an elliptic nose, whose major axis is 12 times the minor axis. A single low-speed streak is produced in a laminar boundary layer by using a small screen of about 2.5 mm height and 7.5 mm width (or 5.5 mm width) set normal to the wall at midspan, and 500 mm downstream of the leading edge. The screen is a 40-mesh

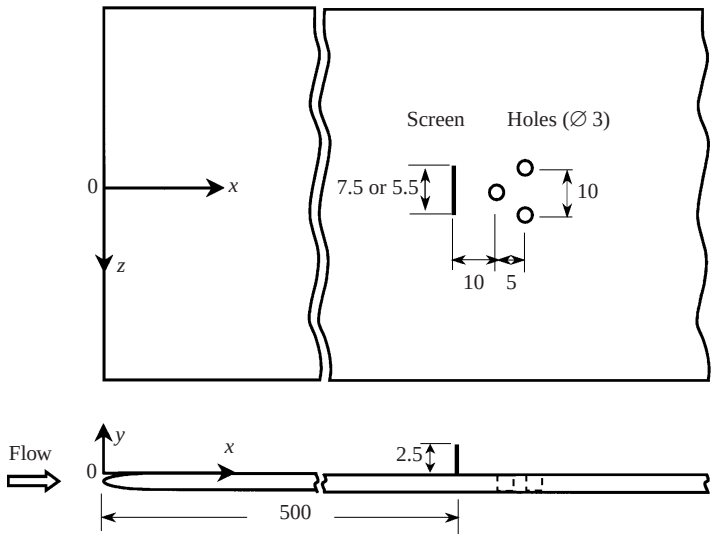

FIGURE 1. Schematic of boundary-layer plate (not to scale). Dimensions in mm.

wire-gauze whose porosity is 0.7. As for the coordinate system, x is the streamwise distance measured from the leading edge, y the normal-to-wall distance, and z the spanwise distance. In the following, the x-position of the screen, $x = 500\,\text{mm}$, is denoted by x_0.

Throughout the present experiment, the free-stream velocity U_∞ is fixed at $4\,\text{m}\,\text{s}^{-1}$. Free-stream turbulence is less than 0.1% at $U_\infty = 4\,\text{m}\,\text{s}^{-1}$. Owing to the cited low background turbulence, a laminar boundary layer develops without the occurrence of any noticeable instability waves in the absence of the streak-generating screen. The velocity distributions without the streak-generating screen are represented well by Blasius flow profiles. The height of the screen is so chosen as to be close to the displacement thickness of the Blasius boundary layer without the screen $\delta_B^* = 2.4\,\text{mm}$ at $x = x_0$ and $U_\infty = 4\,\text{m}\,\text{s}^{-1}$. The Reynolds number based on δ_B^* and U_∞, i.e. $R^* = \delta_B^* U_\infty / \nu$ (where ν is the kinematic viscosity) is about 650 at $x = x_0$. The low-speed streak generated by the screen exhibits inflectional velocity profiles which are approximated well by a hyperbolic-tangent function in the normal-to-wall (y) direction and by wake-type profiles in the spanwise (z) direction, as will be shown later. The boundary-layer spanwise vortex lines coming from upstream are initially straight, but undergo distortions when approaching the screen so that a stationary horseshoe vortex might appear surrounding the screen, with a pair of longitudinal vortices extending downstream. We will describe this point later on the basis of hot-wire measurements.

Unless artificial disturbances (with larger amplitude than background turbulence) are introduced, the boundary layer with the low-speed streak remains completely laminar in the present observation region up to $x - x_0 = 200\,\text{mm}$. This enables us to control the instability of the low-speed streak by using artificial disturbances. In the present experiment, well-controlled artificial disturbances are introduced through small holes. Three holes 3 mm in diameter are drilled through the plate, immediately downstream of the screen. One is at midspan ($z = 0$) at $x - x_0 = 10\,\text{mm}$ and it is used for the excitation of spanwise symmetric disturbances. The other two holes, which are used for the excitation of antisymmetric disturbances, are 10 mm apart in

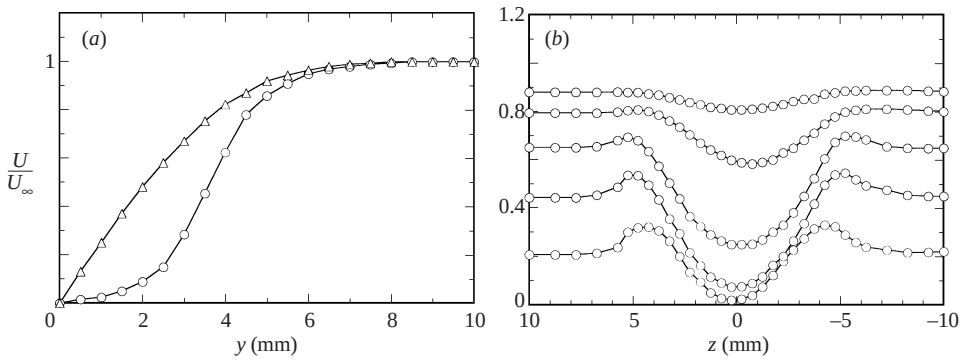

FIGURE 2. The y- and z-distributions of mean velocity U at $x - x_0 = 50$ mm in the case of the 7.5 mm wide screen. (a) y-distributions at ○, $z = 0$; △, $z = 30$ mm. (b) z-distributions at $y = 5$ mm, 4 mm, 3 mm, 2 mm, 1 mm.

the spanwise direction (i.e. $z = \pm 5$ mm) at $x - x_0 = 15$ mm. These three holes are separately connected to three loudspeakers by vinyl hoses. Each loudspeaker is driven at a single frequency through a power amplifier. The antisymmetric disturbances are excited by driving two loudspeakers (connected to the holes at $x - x_0 = 15$ mm) separately with sine-wave signals which are 180° out of phase.

A constant-temperature hot-wire anemometer is used to measure time-mean and fluctuation velocities in the streamwise (x) direction, U and u. The sensitive length of the hot-wire sensor, a tungsten wire of 5 μm in diameter, is 1 mm. The hot-wire probe is traversed in the x-, y- and z-directions. The y-distributions of U and u' (the r.m.s. value of u) are recorded during each y-traverse. The hot-wire signal is also stored in a personal computer. The flow visualization is carried out by means of the smoke-wire technique to identify the excited three-dimensional disturbances. A smoke-wire, stretched in the spanwise direction, can be traversed in the x- and y-directions. The side view, top view and cross-sectional view pictures of the smoke pattern are taken by using a sheet of stroboscopic light, which is synchronized with the forcing signal.

3. Velocity field downstream of the screen

Figures 2(a) and 2(b) illustrate, respectively, the y- and z-distributions of time-mean velocity U at $x - x_0 = 50$ mm in the case of the 7.5 mm wide screen. In figure 2(a), the y-distribution of U is measured at midspan ($z = 0$) and compared with the distribution at $z = 30$ mm where the profile is Blasius-like without the screen. The y-distribution at midspan behind the screen is found to be approximated well by a tanh(y) profile. In figure 2(b), the z-distributions are measured at several heights, $y = 1$ mm, 2 mm, 3 mm, 4 mm and 5 mm. A velocity defect due to the drag of the screen is observed markedly below $y = 4$ mm. The spanwise velocity distributions across the low-speed streak are not unlike that of a usual wake, and the lateral scale of the low-speed streak is here defined as the half-value width l_s used for usual wakes. The half-value width l_s is about 6.5 mm at $x - x_0 = 50$ mm. Here we should note that there does not exist any reversed flow region immediately behind the screen. The absence of reversed flow suppresses vortex shedding of the type observed in the case of an isolated roughness. Besides, we notice that the velocity excess induced at the side edges of the screen by the longitudinal vortices (the two legs of the horseshoe

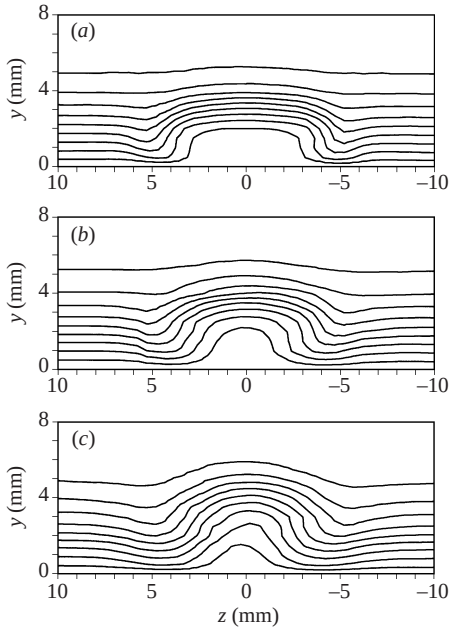

FIGURE 3. The iso-velocity contours in the (y, z)-plane at (a) $x - x_0 = 20$ mm, (b) 50 mm and (c) 100 mm in the case of the 7.5 mm wide screen. Contour levels range from $0.1U_\infty$ to $0.9U_\infty$.

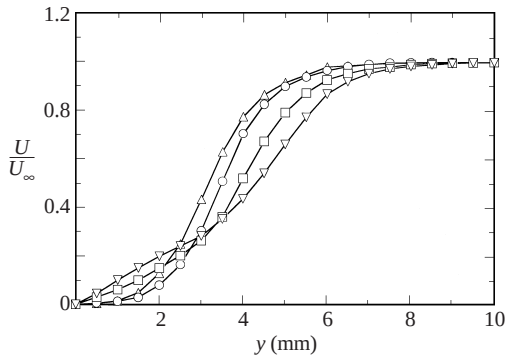

FIGURE 4. The y-distributions of U at $z = 0$ at △, $x - x_0 = 20$ mm; ○, 80 mm; □, 120 mm; ▽, 200 mm in the case of the 7.5 mm wide screen.

vortex mentioned earlier) is small. This indicates that the effect of the stationary horseshoe vortex on the velocity field is really weak. In fact, it is noted that when smoke was released from a smoke-wire stretched close to the wall, the corresponding roll-up of smoke was not observed appreciably. The present low-speed streak is thus almost free of streamwise vorticity in the absence of any artificial disturbances.

Figure 3 illustrates such a laminar low-speed streak in terms of iso-velocity contours in the (y, z)-plane at three x-stations $x - x_0 = 20$ mm, 50 mm and 100 mm. The low-speed streak extends downstream beyond $x - x_0 = 100$ mm though the velocity defect across the low-speed streak fills up gradually with x owing to the momentum transfer by viscous stresses in the lateral as well as normal-to-wall directions. For instance, the velocity difference across the low-speed streak ΔU, measured for the z-distributions of U at $y = 2$ mm or 3 mm, is about 50% and 40% of U_∞ at $x - x_0 = 50$ mm and 100 mm,

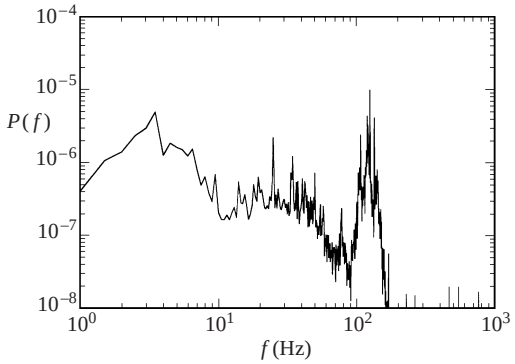

FIGURE 5. Power spectrum of u-fluctuation $P(y)$ at $(x - x_0, y, z) = (200\,\text{mm}, 4.5\,\text{mm}, 0\,\text{mm})$ in the case of the 7.5 mm wide screen.

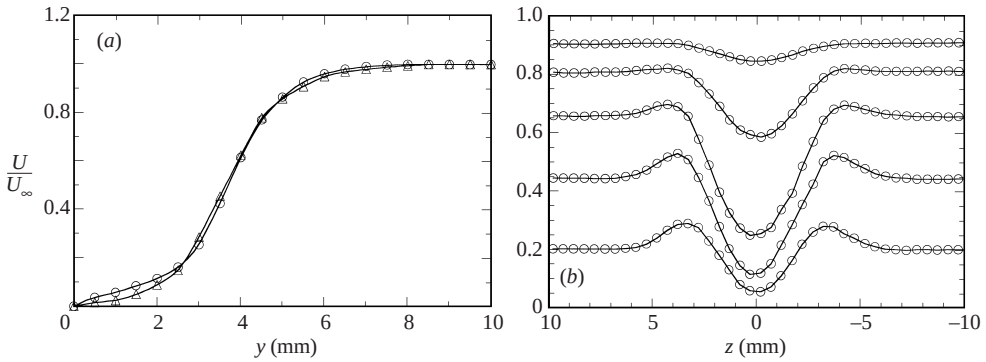

FIGURE 6. The y- and z-distributions of the mean velocity U at $x - x_0 = 50\,\text{mm}$ in the case of 5.5 mm wide screen. (a) y-distributions at $z = 0$ are compared in the two cases (○, the 5.5 mm wide screen; △, the 7.5 mm wide screen). (b) z-distributions at $y = 5\,\text{mm}$, 4 mm, 3 mm, 2 mm, 1 mm.

respectively. Correspondingly, the lateral scale l_s of the low-speed streak decreases slightly with x as the velocity defect is gradually attenuated, the streak width l_s being about 7.5 mm, 6.5 mm and 5 mm at $x - x_0 = 20\,\text{mm}$, 50 mm and 100 mm, respectively. Figure 4 also shows the viscous diffusion of the shear layer (in the y-direction) in terms of the y-distributions of U at midspan ($z = 0$) at $x - x_0 = 40\,\text{mm}$, 80 mm, 120 mm and 200 mm. The velocity gradient in the normal-to-wall (y) direction $\partial U/\partial y$ is decreased down to about 50% between $x - x_0 = 40\,\text{mm}$ and 200 mm, but the velocity profile remains highly inflectional even at $x - x_0 = 200\,\text{mm}$. It is generally expected that the local inflectional velocity profiles (in the y- and z-directions) associated with the low-speed streak are unstable and disturbances undergo exponential growth. However, owing to the cited low background turbulence as well as the weak longitudinal vortices (the two legs of the stationary horseshoe vortex), the low-speed streak remains laminar even beyond $x - x_0 = 200\,\text{mm}$. Figure 5 illustrates the power spectrum of u-fluctuation $P(f)$ (which is scaled with U_∞^2), measured at the maximum shear position at midspan, i.e. $(x - x_0, y, z) = (200\,\text{mm}, 4.5\,\text{mm}, 0\,\text{mm})$. We can see a distinct peak slightly above 100 Hz, which no doubt indicates the presence of instability waves amplified by the inflectional instability. The magnitude of the instability waves is not so large; it is only of the order of 1% in terms of the maximum r.m.s. value of u-fluctuations u'_m/U_∞ at $x - x_0 = 200\,\text{mm}$.

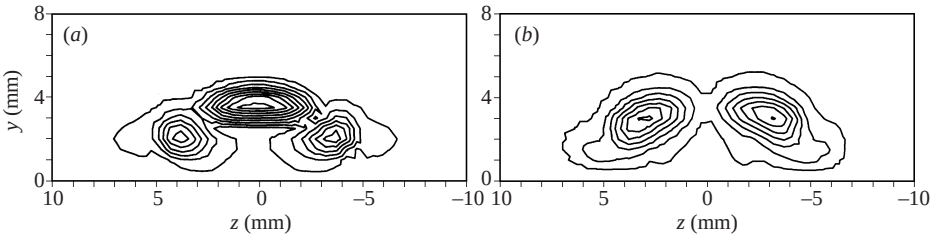

FIGURE 7. The amplitude distribution of u-fluctuation (u_0') in the (y,z)-plane at $x - x_0 = 50\,\text{mm}$ in the case of the 7.5 mm wide screen. (a) Symmetric (varicose) mode of 110 Hz, represented by iso-intensity lines of $u_0'/U_\infty = 0.002$ to 0.018. (b) Anti-symmetric (sinuous) mode of 60 Hz, represented by iso-intensity lines of $u_0'/U_\infty = 0.00025$ to 0.00175.

Similar velocity measurements were made in the case of the 5.5 mm wide screen. Figures 6(a) and 6(b) illustrate, respectively, the y- and z-distributions of the mean velocity U at $x - x_0 = 50\,\text{mm}$ in the case of the 5.5 mm wide screen. Figure 6(a) includes $U(y)$ for the 7.5 mm wide screen, for comparison. The lateral scale of the low-speed streak is 73% of that for the 7.5 mm wide screen, but the velocity gradient in the y (normal-to-wall) direction $\partial U/\partial y$ is almost the same as that for the 7.5 mm wide screen at midspan. Thus, there is no appreciable difference between the two cases except the lateral scale of the low-speed streak.

4. Instability of a low-speed streak

First examined is the linear instability of the three-dimensional high-shear layer associated with the low-speed streak developing behind the 7.5 mm wide screen. Considering the general instability properties of inflectional velocity profiles in the y- and z-directions, we expect that the low-speed streak may grow two kinds of instability mode, i.e. a symmetric varicose mode developing into symmetric hairpin-shaped vortices with a pair of counter-rotating streamwise vortices and an anti-symmetric sinuous mode leading to the meandering of the streak. In order to excite these two kinds of instability mode separately, well-controlled external disturbances are introduced into the laminar low-speed streak through small holes connected to loudspeakers as already mentioned. Figure 7(a) illustrates the amplitude distribution of u-fluctuations u_0' in the (y,z)-plane at $x - x_0 = 50\,\text{mm}$ for the symmetric mode. Here, the forcing frequency f_0 is set at 110 Hz which is close to the most amplified frequency under natural disturbance conditions (see figure 5), and u_0' is the r.m.s. value of the u-fluctuation component at the forcing frequency. As seen from the mean velocity distribution in the (y,z)-plane $U(y,z)$, at the corresponding x-position in figure 3(b), the amplitude distribution u_0' takes the largest values in the horizontal shear layer at a height $y = 3.5\,\text{mm}$ where the velocity gradient in the normal-to-wall direction $\partial U/\partial y$ takes a maximum, and in the vertical shear layer around $z = \pm 3.5\,\text{mm}$ where the spanwise velocity gradient $\partial U/\partial z$ becomes the largest. Figure 7(b) illustrates the antisymmetric mode in terms of the (y,z)-plane map of u_0', obtained with a forcing frequency f_0 of 60 Hz. The amplitude distribution of the antisymmetric mode is symmetric with respect to midspan ($z = 0$), but its phase undergoes a 180° jump across midspan and therefore the amplitude vanishes at $z = 0$. Here, we obtained similar amplitude distributions for each mode at various x-stations. Besides, we measured the phase velocity of each mode and confirmed that it is almost constant across the boundary layer at any spanwise position, $0.4U_\infty$ and $0.5U_\infty$ for the

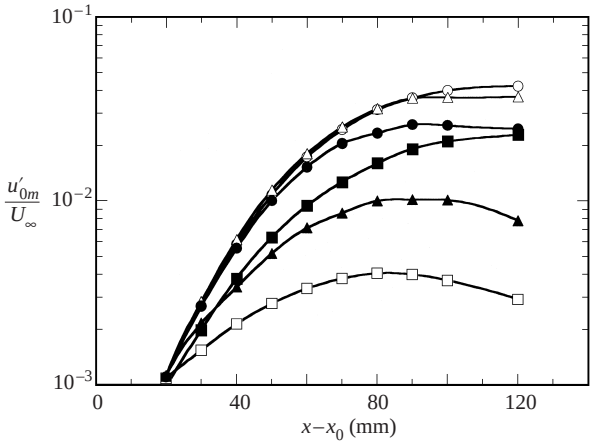

FIGURE 8. Streamwise development of the symmetric mode in the case of the 7.5 mm wide screen. □, 40 Hz; ■, 80 Hz; ○, 110 Hz; △, 120 Hz; ●, 140 Hz; ▲, 170 Hz.

symmetric mode and the antisymmetric mode, respectively. Thus, the excited waves are identified as the eigenmodes of the three-dimensional shear layer associated with the low-speed streak. Note that the phase speeds of the symmetric and antisymmetric modes are close to the local velocity at the inflection points in the y-distribution of U at $z = 0$ and in the z-distribution at $y = 3$ mm, respectively. The velocity shear ($\partial U/\partial y$ or $\partial U/\partial z$) becomes largest at these inflection points. In the following, the instability characteristics of these two modes are examined in detail.

Figure 8 illustrates the streamwise development of the symmetric mode excited at a frequency in the range of 40–170 Hz, in terms of u'_{0m}, the y-maximum of u'_0 at each x-station. Beyond the transient (or receptivity) region up to $x - x_0 = 20$–30 mm, the excited waves undergo exponential growth. In each case, the initial wave amplitude is set at a sufficiently small value so as to observe the linear instability. The frequency-selective growth of disturbances is very clear and the largest amplification occurs around 110 Hz in the region up to $x - x_0 = 70$ mm. Beyond this region, the growth of all the symmetric disturbances becomes slow. This is due to nonlinear effects and/or viscous diffusion of the shear layer. Nonlinear effects might appear beyond $x - x_0 = 70$ mm for $f_0 = 110$, 120 and 140 Hz because the amplitude already attains a few per cent of the free-stream velocity around that station. However, we measured the growth curve of the 110 Hz disturbance with still smaller amplitudes, and we confirmed that the behaviour given in figure 8 is essentially in a linear stage of development. Therefore, the decrease in growth rate is attributed to the decrease in the spanwise scale of the lifted high-shear layer due to viscous diffusion; see figure 3 which demonstrates the downstream changes in the low-speed streak velocity fields. For the case of the disturbance at $f_0 = 40$ Hz, the streamwise growth is much affected by the limited spanwise extent of the shear layer. It is reasonable to consider that lower-frequency disturbances with a longer wavelength are more affected by the three-dimensionality of the low-speed streak. Indeed, the spanwise scale of the uplifted shear layer is about 6.5 mm at $x - x_0 = 50$ mm but decreases down to about 5.0 mm at $x - x_0 = 100$ mm, which is about one-tenth of the wavelength of the 40 Hz disturbance (about 50 mm). The effect of the streak width (or the spanwise scale of the uplifted shear layer) on the growth of the symmetric modes is discussed again later.

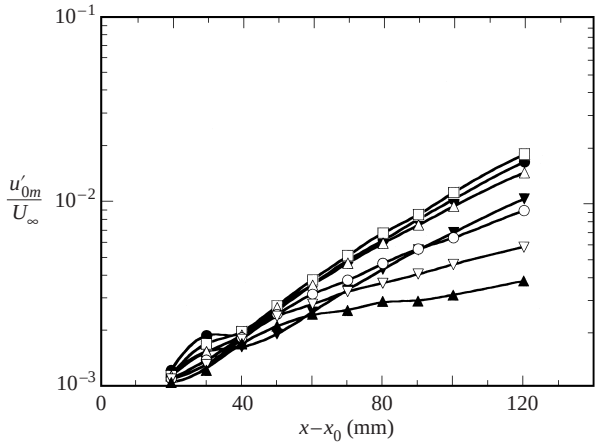

FIGURE 9. Streamwise development of the antisymmetric mode in the case of the 7.5 mm wide screen. ▼, 40 Hz; ●, 50 Hz; □, 60 Hz; △, 70 Hz; ○, 80 Hz; ▽, 90 Hz; ▲, 100 Hz.

Figure 9 illustrates the streamwise development of u'_{0m} for the antisymmetric modes. The most amplified antisymmetric mode occurs at $f_0 = 50$–60 Hz. Its spatial growth rate $-\alpha_i (= \mathrm{d}[lnu'_{0m}]/\mathrm{d}x)$ is much less than that of the most amplified symmetric mode (110 Hz). For instance, by estimating the spatial growth rate at $x - x_0 = 50$ mm, we obtain $-\alpha_i = 0.06\,(\mathrm{mm}^{-1})$ for the most amplified symmetric mode and $-\alpha_i = 0.03\,(\mathrm{mm}^{-1})$ for the most amplified antisymmetric mode. Thus, the maximum growth rate of the antisymmetric mode is half the value of the symmetric mode at this x-station. In contrast to the symmetric modes whose growth rates are decreased downstream, each antisymmetric mode continues to grow exponentially with an almost constant growth rate even beyond $x - x_0 = 100$ mm. In other words, the antisymmetric modes can grow and survive much longer than the symmetric modes, although their growth rates are smaller than those of the symmetric modes in the early stages. Here, it should be noted that the growth curves (u'_{0m} *vs.* x) in figure 9 are wavy, in particular for $x - x_0 < 50$ mm. The wavy behaviour no doubt reflects the receptivity process generating the eigenmodes. According to our experience, the wavy behaviour becomes faint when the excited disturbance has a large growth rate, as seen from figure 8 for the symmetric disturbances.

The instability characteristics such as the growth rates depend on the three-dimensional structure of the low-speed streak, i.e. its lateral width and vertical height relative to the shear-layer thickness. The thickness of the horizontal shear layer, defined as $\delta U/(\partial U/\partial y)_i$ where $(\partial U/\partial y)_i$ is $\partial U/\partial y$ at the inflection point and δU is the velocity difference across the horizontal shear layer ($\delta U \sim U_\infty$ in the present case), is about 2.5 mm at $x - x_0 = 50$ mm. Therefore, the lateral width of the horizontal shear layer, about 6.5 mm around $x - x_0 = 50$ mm, is about 2.5 times the shear-layer thickness. At $x - x_0 = 100$ mm where the growth rate of the symmetric mode is remarkably reduced, the ratio of the streak width (about 5 mm) to the shear-layer thickness (about 3.5 mm) is decreased to about 1.5. We can then imagine that when the low-speed streak is produced behind a narrower screen, the growth rate of the symmetric mode becomes much smaller. So, to see the effect of the lateral scale of the low-speed streak on the growth rates, similar measurements are carried out for the 5.5 mm wide screen with the height unchanged. The velocity gradient in the y-direction is almost the same at midspan for the two cases (5.5 mm wide screen and 7.5 mm wide

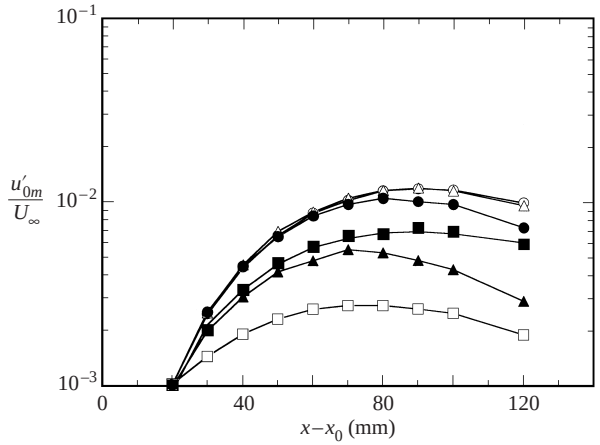

FIGURE 10. Streamwise development of the symmetric mode in the case of the 5.5 mm wide screen. □, 40 Hz; ■, 80 Hz; ○, 110 Hz; △, 120 Hz; ●, 140 Hz; ▲, 170 Hz.

screen), as already shown in figure 6. Figure 10 illustrates the streamwise development of u'_{0m} for the symmetric mode at various frequencies in the case of the 5.5 mm wide screen. The frequency of the most amplified symmetric mode is almost the same as before, i.e. about 110 Hz, but its growth rate is definitely reduced compared with the case of the 7.5 mm wide screen. That is, the maximum growth rate in the case of the 5.5 mm wide screen is found to be about 0.03 (mm^{-1}) at $x - x_0 = 50$ mm, nearly half the value in the case of the 7.5 mm wide screen. Besides, all the disturbances cease to grow beyond $x - x_0 = 80$ mm, where the ratio of the streak width to the shear-layer thickness approaches unity. Note that the disturbance is small enough in amplitude to exhibit linear behaviour, that is, u'_{0m}/U_∞ is less than 1%. Thus, it is important to stress that by decreasing the streak width relative to the shear-layer thickness, the streak becomes stable to symmetric disturbances. The critical streak width for the growth of the symmetric modes is found to be of the order of the shear-layer thickness in the two cases of 5.5 mm and 7.5 mm wide screens.

To understand the instability characteristics in more detail, stability calculations were made for the y-distribution of U (at midspan) at $x - x_0 = 50$ mm on the basis of the Orr–Sommerfeld stability equation (under parallel flow assumption). Here, it is noted that the velocity profile $U(y)$ at midspan is very approximated well by a tangent-hyperbolic profile. Figure 11(a) illustrates the variations of the spatial growth rate of the symmetric mode with the frequency and compares them with the stability calculations. The comparison clearly indicates that the frequency of the most amplified disturbance is predicted well by the Orr–Sommerfeld stability calculation for the inflectional profile $U(y)$. As for the growth rate, however, we see a rather poor agreement. The maximum growth rates obtained experimentally in the two cases of the 7.5 mm wide screen and the 5.5 mm wide screen are about 60% and 35% of that calculated from the Orr–Sommerfeld equation, respectively. Figure 11(b) compares the wavenumber α_r measured around $x - x_0 = 50$ mm for the two cases with the Orr–Sommerfeld result; the experimental result coincides with the stability calculation. This reveals that the wavenumber of the instability mode is little affected by the spanwise variations in the inflectional velocity profile.

Figure 12 illustrates the streamwise development of u'_{0m} for the antisymmetric modes of various frequencies for the 5.5 mm wide screen. We can see that each disturbance

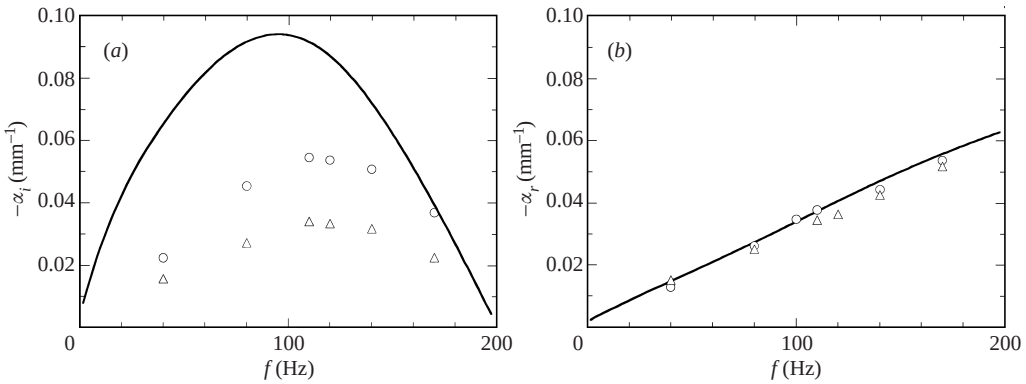

FIGURE 11. Spatial growth rate $-\alpha_i$ and wavenumber α_r of the symmetric mode at $x - x_0 = 50$ mm. ○, the 7.5 mm wide screen; △, the 5.5 mm wide screen; —, the Orr–Sommerfeld equation.

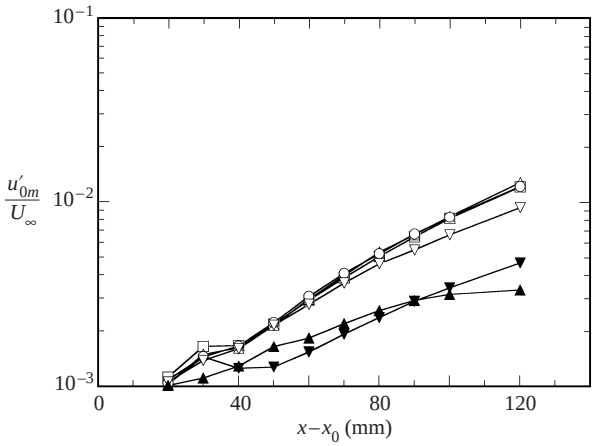

FIGURE 12. Streamwise development of the antisymmetric mode in the case of the 5.5 mm wide screen. ▼, 40 Hz; □, 60 Hz; △, 70 Hz; ○, 80 Hz; ▽, 90 Hz; ▲, 100 Hz.

grows exponentially with an almost constant growth rate in this case too. The most amplified antisymmetric disturbance occurs at around 70–80 Hz, which is higher than that for the 7.5 mm wide screen (50–60 Hz) by 30%. Thus, the growth rate curve ($-\alpha_i$ *vs.* frequency) moves towards higher frequencies by about 20 Hz (30%). The increase in the most amplified frequency results from the decrease in the width of the low-speed streak as the screen width changes from 7.5 mm to 5.5 mm. Generally speaking, for the instability of wake-type velocity profiles, the frequency of the most amplified mode is in inverse proportion to the wake width. This is also the case in the present streak flow. That is, the lateral scale l_s for the 5.5 mm wide screen is about 4.5 mm at $x - x_0 = 50$ mm and therefore about 70% of that for the 7.5 mm wide screen. The dependence of the growth rate on the streak width is more clearly shown in figure 13 which compares the growth rates for the two screen widths. The growth rates are estimated at $x - x_0 = 50$ mm to 70 mm in a region where they are almost constant for all the frequencies. We also see that the maximum growth rate is about 0.03 (mm^{-1}) for the two cases. It is interesting that this maximum is almost the same as that of the symmetric mode (at $x - x_0 = 50$ mm) in the case of the 5.5 mm wide screen. Therefore, we may say that when the ratio of the streak width to the shear-layer thickness is less

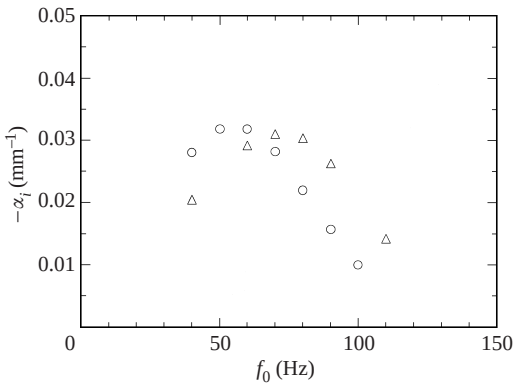

FIGURE 13. Spatial growth rate $-\alpha_i$ of the antisymmetric mode at $x - x_0 = 50$–70 mm. ○, the 7.5 mm wide screen; △, the 5.5 mm wide screen.

than about 1.5, the antisymmetric mode is more dangerous than the symmetric mode. Here, we should note that the Orr–Sommerfeld equation assuming two-dimensional flow cannot predict well the growth rates of antisymmetric modes. This is because the limited vertical height of the low-speed streak causes rapid changes in the spanwise wake profile with distance from the wall. In order to make accurate comparisons between the experiment and stability theory, a three-dimensional stability calculation for the two-dimensional inflectional velocity distribution $U(y, z)$ has to be done, as has been carried out by Hall & Horseman (1991), Yu & Liu (1991) and Park & Huerre (1994) for the secondary instability of Görtler vortices. Although such a stability calculation is not carried out in the present study, the essential features of the streak instability are well understood from the present experimental results.

5. Development of instability waves into coherent vortices

From the above results, we understood the linear instability of the three-dimensional shear layer associated with a low-speed streak. Our next interest is to see how the instability modes evolve into coherent vortices to lead to wall turbulence. First, let us show the development of the two instability modes by means of smoke-wire visualization in the case of the 7.5 mm wide screen. The forcing amplitudes were increased ten times when compared with those for the case of the linear stability experiment in order to reach the nonlinear and later stages of the disturbance development in the observation region up to $x - x_0 = 200$ mm, as illustrated in figure 14. We can see that the antisymmetric mode can continue its exponential growth until the amplitude u'_m (the r.m.s. value of u-fluctuations) exceeds about 10% of the free-stream velocity. On the other hand, as already shown in figure 10, the linear instability of symmetric modes is inhibited when the shear-layer thickness becomes comparable with the streak width. So, the symmetric mode cannot evolve into discrete vortices if the initial amplitude is weak. When the initial amplitude is large enough, the symmetric mode can grow into discrete vortices before the shear layer has diffused as shown in figure 14.

Figures 15 and 16 show the evolution of the symmetric (varicose) mode at 110 Hz and of the antisymmetric (sinuous) mode at 60 Hz, respectively, in terms of top view pictures from smoke-wire visualizations. For the three photographs in each figure, smoke was released from a smoke-wire stretched in the spanwise direction at

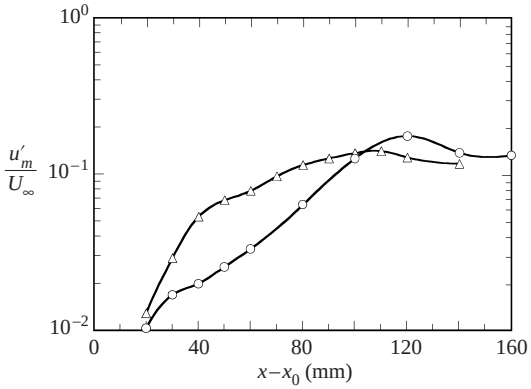

FIGURE 14. Maximum r.m.s. amplitude u'_m against x in the case of the 7.5 mm wide screen. △, symmetric mode; ○, antisymmetric mode.

$y = 4$ mm, 3 mm and 2 mm, respectively. These pictures are still-camera shots but the stroboscopic light is synchronized with the forcing signal so as to obtain the flow pattern at the same phase in the forcing cycle. The visualization pictures in figure 15 indicate that the symmetric mode soon evolves into a train of discrete vortices beyond $x - x_0 = 80$ mm which then lead to the formation of a turbulent wedge. Figure 17 shows the development of such symmetric vortices by means of a cross-sectional view from smoke-wire visualizations. The stroboscopic light sheet (synchronized with the forcing signal) illuminates the y–z cross-section at $x - x_0 = 85$ mm. The eight photographs were taken at intervals of one eighth of the forcing period and they cover one whole forcing cycle ($f_0 = 110$ Hz). We can see the development of a pair of symmetric, counter-rotating streamwise vortices over half a period clearly. In other words, the visualization pictures in figures 15 and 17 clearly indicate the occurrence of symmetric hairpin-shaped vortices, as has been shown through a visualization study of the development and regeneration of hairpin vortices by Haidari & Smith (1994).

Here, the forced flows are so periodic, as far as the excited vortices are concerned, that the ensemble-averaged velocity field obtained by phase averaging can reproduce the instantaneous flow field very well at least up to $x - x_0 = 200$ mm. Figure 18 illustrates the ensemble- (phase-) averaged velocity field under the symmetric mode excitation in terms of iso-velocity contours in the (x, z)-plane at a height $y = 3$ mm (corresponding to figure 15). The interval in the time sequence is a quarter of the forcing period $T(= 1/f_0)$. We see that the rapid growth of the symmetric mode causes the single low-speed streak to develop into a varicose structure which subsequently gives rise to a pair of low-speed lumps in each cycle. The pair of low-speed lumps no doubt corresponds to the passage of the two legs of a hairpin vortex or a pair of counter-rotating quasi-streamwise vortices located at around $z = \pm 2.5$ mm. Figure 19 illustrates the ensemble-averaged velocity field in the (y, z)-plane at $x - x_0 = 85$ mm; the near-wall low-speed fluid is lifted up by each streamwise vortex, i.e. each leg of the hairpin vortex. Smith *et al.* (1991) and Haidari & Smith (1994) explained that the ejection of low-speed fluid was caused by the wall pressure gradient induced by each leg of the hairpin vortex, in reference to the vortex-induced unsteady separation analysed theoretically by Dommelen & Cowley (1990) and Peridier, Smith & Walker (1991*a*, *b*). Besides, we can observe that being associated with the lift-up of near-wall fluid, each hairpin leg itself evolves into a pair of counter-rotating streamwise vortices at x-stations slightly downstream. For instance, figure 20 shows the cross-

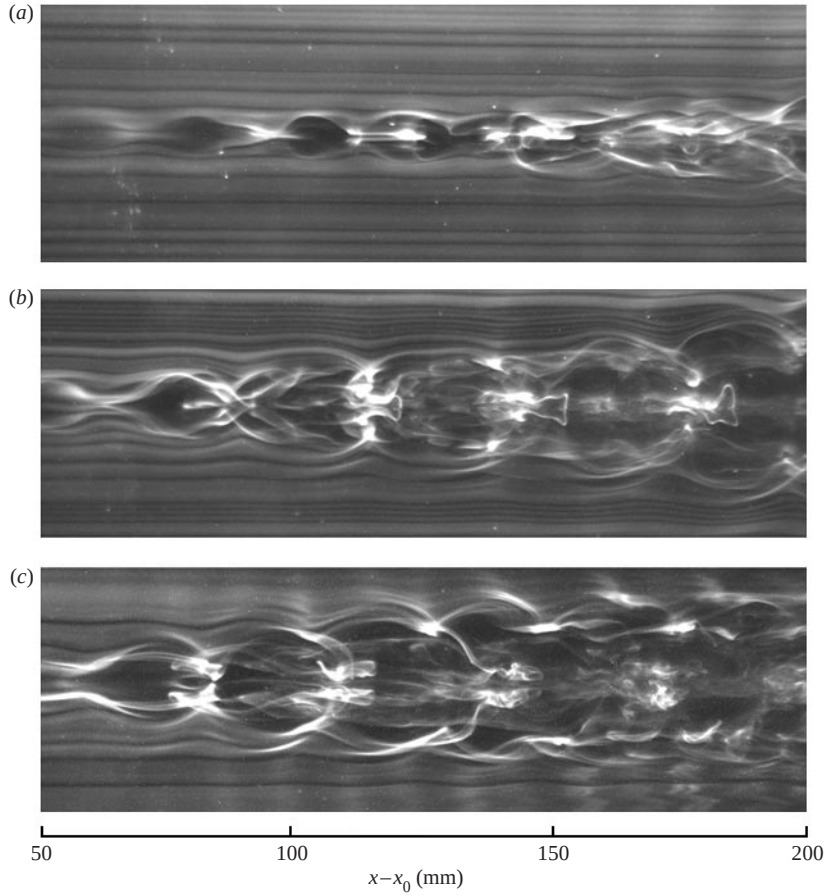

FIGURE 15. Visualization of the development of symmetric mode (110 Hz) in the case of the 7.5 mm wide screen. Smoke is released from (*a*) $y = 4$ mm, (*b*) 3 mm and (*c*) 2 mm.

sectional view at $x - x_0 = 110$ mm, where four pictures complete one period of the forcing. The smoke-wire is stretched close to the wall (at $x - x_0 = 65$ mm) so as to visualize the generation of near-wall vortices. The smoke released from the smoke-wire near the wall rolls up into a mushroom-shaped structure over half the period at around $z = \pm 2.5$ mm. This no doubt indicates that each leg of the primary hairpin vortex (located at $z = \pm 2.5$ mm) develops into a pair of counter-rotating streamwise vortices. Here, the head of the primary hairpin vortex is soon diffused (not visible in the pictures) and seems to play no important role in the regeneration of hairpin vortices. It should also be noted that further downstream, new low-speed streaks occur and soon evolve into hairpin vortices on both sides of the primary hairpin vortices, which leads to lateral contamination in a turbulent wedge, as visualized in experiments on the successive development of hairpin vortices by Acarlar & Smith (1987*a*, *b*), Smith *et al.* (1991), Haidari & Smith (1994), Asai *et al.* (1996) and Asai & Nishioka (1997).

As for the antisymmetric mode, we can see in figure 16 that the growth of the instability waves leads to the meandering of the low-speed streak near the wall and the appearance of a vortex street not unlike the Kármán vortex street away from a wall. In addition, diffused smoke along the streak beyond $x - x_0 = 150$ mm suggests

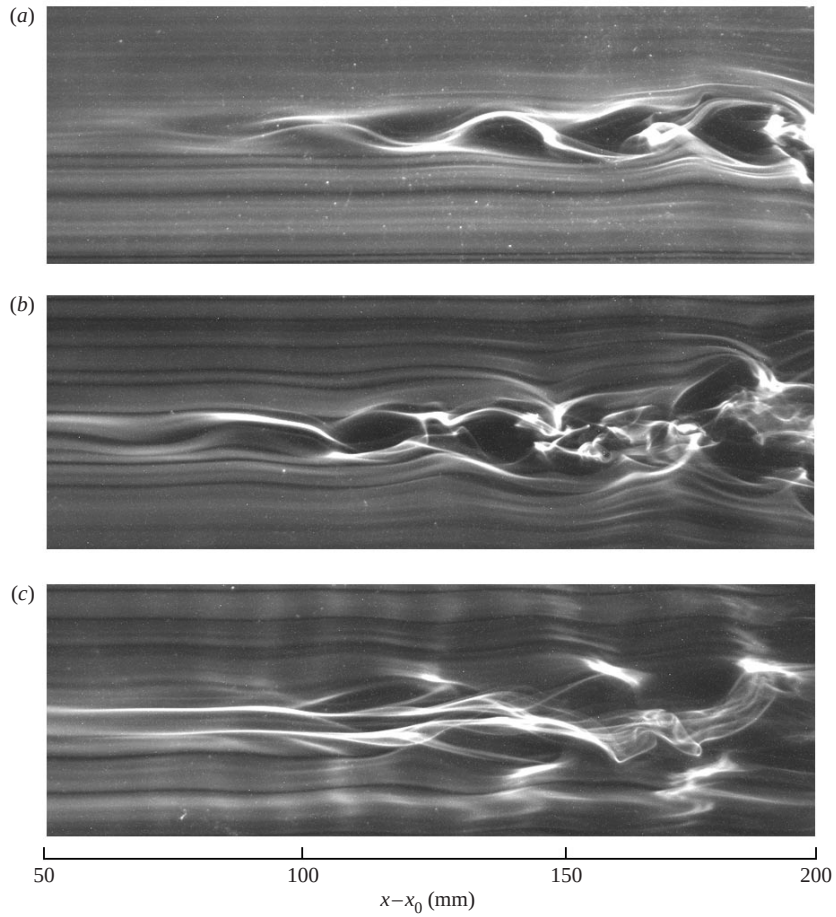

FIGURE 16. Visualization of the development of the antisymmetric mode (60 Hz) in the case of the 7.5 mm wide screen. Smoke is released from (*a*) $y = 4$ mm, (*b*) 3 mm and (*c*) 2 mm.

the occurrence of further breakdown of the meandering streak into smaller scale eddies. To see such meandering of the streak more clearly, figure 21 illustrates the ensemble-averaged velocity field in terms of a time sequence of iso-velocity contours in the (x, z)-plane at a height $y = 3$ mm where the amplitude of the u-fluctuation component becomes maximum. Correspondingly, figure 22 illustrates a time sequence of iso-velocity contours in the (y, z)-plane at $x - x_0 = 140$ mm. From these figures, we also recognize that the instability is essentially of wake-type though it strongly suffers from no-slip wall effects and mean shear effects. These velocity patterns are quite similar to those of the near-wall streaky structure obtained from DNS data of wall turbulence by the VISA conditional sampling technique (Johansson *et al.* 1991). In the present case, the amplitude of the antisymmetric mode grows exponentially to a value greater than 10% of U_∞ in terms of the maximum r.m.s. value of u-fluctuations beyond $x - x_0 = 80$ mm, and it saturates due to nonlinear effects around $x - x_0 = 120$ mm (see figure 14). Correspondingly, the meandering of the low-speed streak appears appreciably beyond $x - x_0 = 80$ mm and the sinuous structure of the streak instability is established beyond $x - x_0 = 120$ mm.

The meandering of the streak results in the generation of a train of streamwise vortices convecting downstream, as clearly visualized in the (y, z)-cross-sectional view

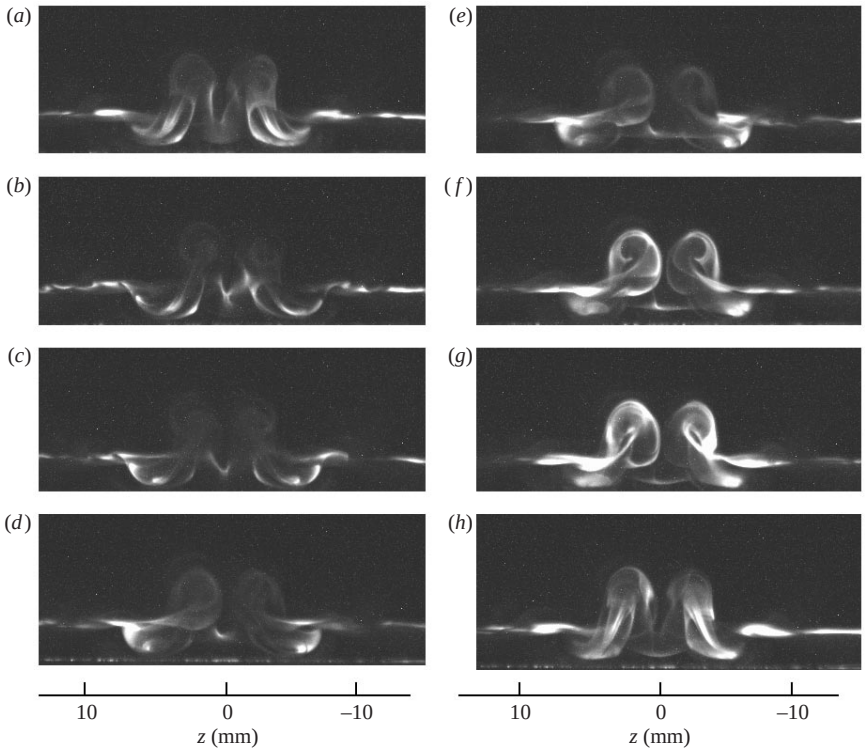

FIGURE 17. Visualization of the development of the symmetric mode (110 Hz) in the case of the 7.5 mm wide screen. Cross-sectional view at $x - x_0 = 85$ mm. Time interval between pictures is one-eighth of the forcing period.

of figure 23 at $x - x_0 = 160$ mm. Here, the smoke released from an x-station 50 mm upstream of the observation station x, visualizes active vortical structures. The near-wall smoke rolls up and moves in the left and right directions alternately during one cycle, showing the formation of a quasi-streamwise vortex with vorticity of alternate sign in each half cycle. We may infer that the wake-type instability excites a vortex array of the y- (normal-to-wall) vorticity component and simultaneously the tilting of the y-vorticity component due to the mean shear $\partial U/\partial y$ generates the observed quasi-streamwise vortices. Such an array of travelling quasi-streamwise vortices is quite similar to that deduced by Jeong *et al.* (1997) from DNS data of wall turbulence. From the top view visualization picture and the iso-velocity contours in the (x, z)-plane, the tilting angle of the low-speed streak is found to be about 5° at $y = 2$ mm and about 10° at $y = 3$ mm at the stage of vortex formation around $x - x_0 = 120$ mm. Note that we obtained the iso-velocity contours at $y = 2$ mm too. We examined the tilting angle of the low-speed streak for the case of the narrower streak produced by the 5.5 mm wide screen, and found that the tilting angle of the low-speed streak was almost the same as for the 7.5 mm wide screen. From the cross-sectional view pictures, we see that the tilted streamwise vortices appear around $y = 2$ mm. Therefore, by estimating the tilting angle of streamwise vortices as that of the streak at $y = 2$ mm, we find a tilting angle of about 5°, which is also the same as that found in wall turbulence by Jeong *et al.* (1997). As these coherent vortices develop downstream, further breakdown of the convecting vortices into higher-frequency smaller-scale eddies occurs along the tilted quasi-streamwise

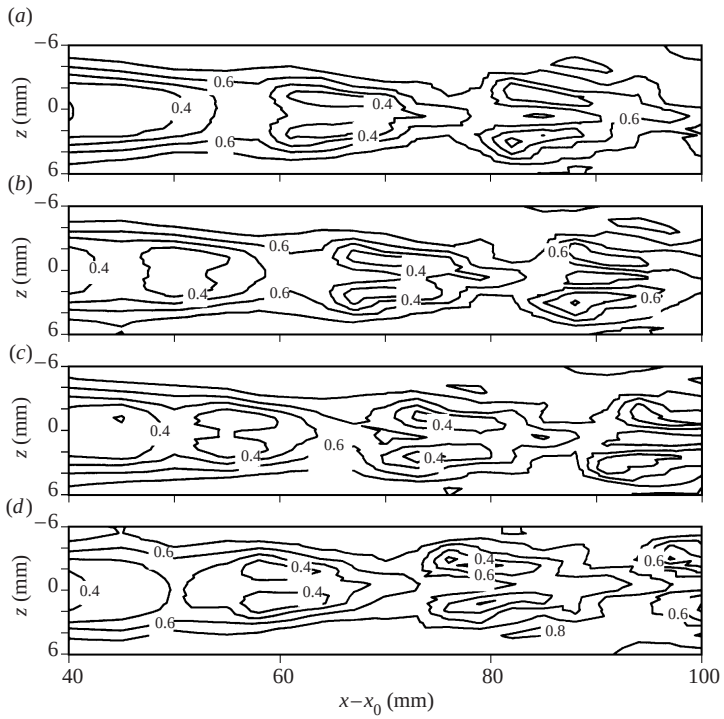

FIGURE 18. Ensemble-averaged velocity field under the excitation of the symmetric mode (110 Hz) in the (x, z)-plane at a height $y = 3$ mm in the case of the 7.5 mm wide screen. Time t/T is (a) 0, (b) $\frac{1}{4}$, (c) $\frac{2}{4}$, (d) $\frac{3}{4}$.

vortices, as seen from the diffused smoke in the visualization pictures of figure 16. We followed up the development of these vortices further downstream and found that even after the occurrence of such a secondary instability, the meandering low-speed streak was maintained as the most dominant periodic near-wall activity at least over a few wavelengths in the observation region. The detailed investigation of the final evolution of the streak instability modes into wall turbulence is in progress.

6. Concluding remarks

In the present experimental study, a single low-speed streak was produced in a Blasius boundary layer by using a small piece of screen (a wire-gauze) to examine its instability characteristics and the resulting generation of coherent vortices. The stationary streamwise vortices associated with the low-speed streak behind the screen were very weak, and thus the streak was considered to be almost free of streamwise vorticity in the present experiment. Furthermore, owing to low background noise as well as low Reynolds numbers, the low-speed streak remained completely laminar throughout the observation region. This enabled us to study the linear and nonlinear instability process of the low-speed streak in detail by introducing well-controlled artificial disturbances. The excited symmetric (varicose) mode was found to be essentially governed by the Kelvin–Helmholtz instability of the inflectional velocity profile in the normal-to-wall direction. The most unstable frequency did not much depend on the spanwise scale of the streak, but the growth rate was found to decrease with

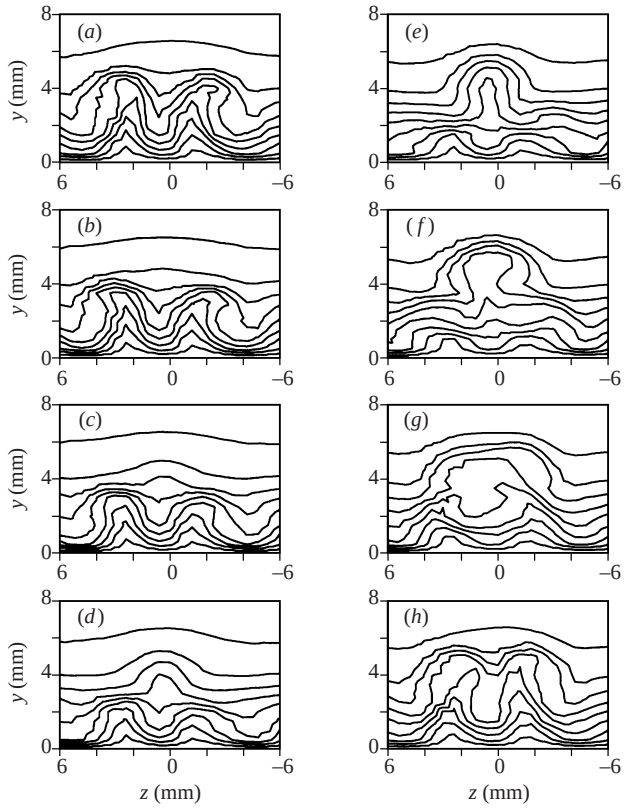

FIGURE 19. Ensemble-averaged velocity field under the excitation of the symmetric mode (110 Hz) in the (y, z)-plane at $x - x_0 = 85$ mm in the case of the 7.5 mm wide screen. Time t/T is (*a*) 0, (*b*) $\frac{1}{8}$, (*c*) $\frac{2}{8}$, (*d*) $\frac{3}{8}$, (*e*) $\frac{4}{8}$, (*f*) $\frac{5}{8}$, (*g*) $\frac{6}{8}$, (*h*) $\frac{7}{8}$. Velocity levels range from $0.1U_\infty$ to $0.9U_\infty$.

the width of the low-speed streak, i.e. the spanwise extent of the uplifted horizontal $(\partial U/\partial y)$ shear layer. In fact, when the width was twice the shear-layer thickness, the maximum growth rate was reduced by 40% as compared with that of a two-dimensional shear-layer instability. The viscous diffusion of the shear layer thus reduces the growth rate of the symmetric (varicose) mode at downstream stations by decreasing the spanwise width of the lifted shear layer relative to its thickness. When the shear-layer thickness approaches the streak width at some downstream station, the symmetric modes cease to grow. On the other hand, for the antisymmetric (sinuous) mode associated with the wake-type profile across the low-speed streak, the growth rate was not so strongly affected by a decrease in the streak width. So, compared with the symmetric modes, the antisymmetric modes can grow exponentially further downstream. In this regard, Schoppa & Hussain (1997, 2000) stressed, through a numerical simulation of the linear instability of the low-speed streaks (deduced from the DNS data of wall turbulence), that viscous diffusion of the streak was crucial even for the growth of the antisymmetric sinuous mode. Indeed, the disturbance energy grows only three-fold until the near-wall streaks are diffused owing to viscosity in their simulation. Whereas, the disturbance can grow by one order of magnitude in terms of u'_m in the present streak. This difference between their simulation and the present experiment is no doubt attributable to the differences in the velocity profiles (across the low-speed streak) as well as the related Reynolds

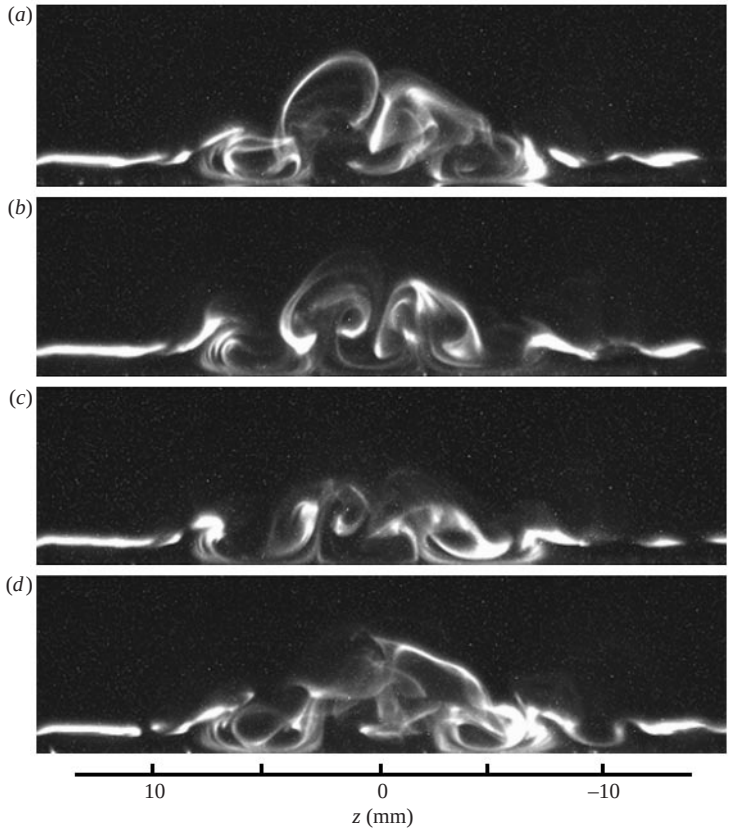

FIGURE 20. Visualization of the development of the symmetric mode (110 Hz) in the case of the 7.5 mm wide screen. Cross-sectional view at $x - x_0 = 110$ mm. Time interval between pictures is a quarter of the forcing period.

number. In our experiment, the Reynolds number R_s, based on the streak width l_s and the velocity difference across the streak ΔU, is greater than 450 at 100 mm downstream of the screen, even for the case of the narrower (5.5 mm wide) screen. In the numerical simulation of Schoppa & Hussain, the streak instability ceases to grow when the velocity defect ΔU scaled with the friction velocity u_τ becomes less than 7.6. This indicates that the critical value of R_s for the streak instability is 380 for the streak width $50\nu/u_\tau$ (i.e. half the spacing of the typical streaks in wall turbulence). The value R_s of the present streak is thus greater than the critical R_s in the numerical simulation, and we could observe the exponential growth of the antisymmetric (sinuous) mode up to the nonlinear saturation stage in the present low-speed streak experiment. It is expected that when the disturbance triggering the streak instability is strong, a similar disturbance development should be observed in near-wall turbulence.

When the excited instability waves are amplified, they can evolve into coherent vortices leading to wall turbulence. The growth of the symmetric (varicose) mode leads to the formation of hairpin-shaped vortices with a pair of counter-rotating streamwise vortices, while the antisymmetric (sinuous) mode develops into travelling quasi-streamwise vortices not unlike those found in the near-wall region of developed turbulent flows. The streamwise vorticity associated with the present low-speed

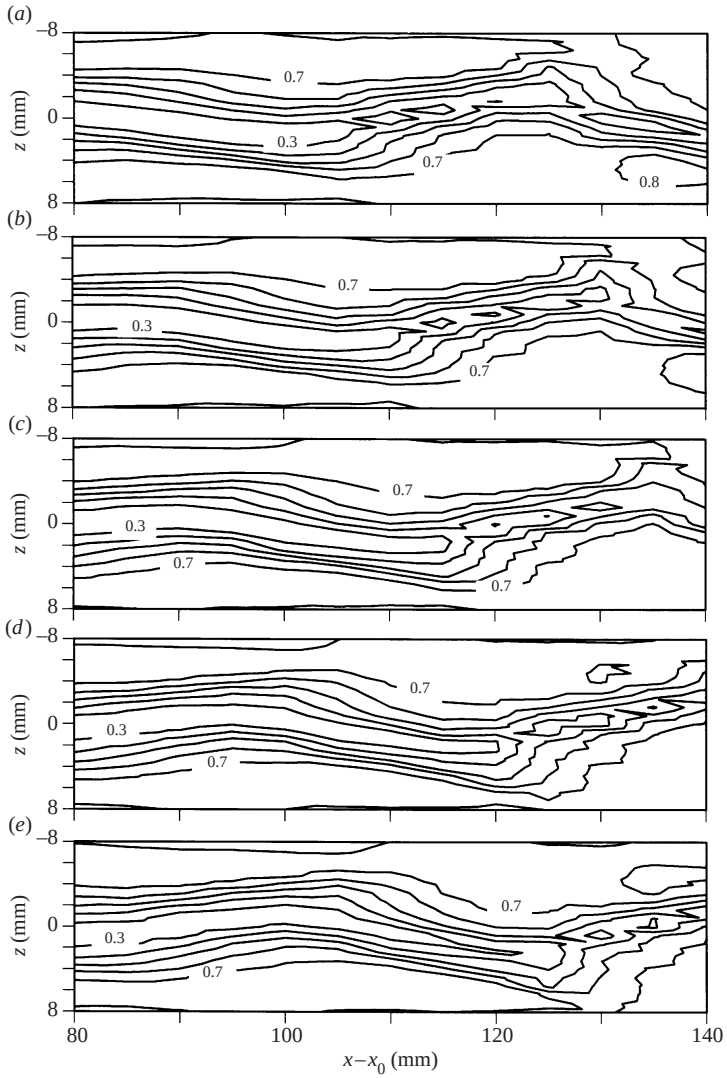

FIGURE 21. Ensemble-averaged velocity field under the excitation of the antisymmetric mode (60 Hz) in the (x, z)-plane at $y = 3$ mm in the case of the 7.5 mm wide screen. Time t/T is (*a*) 0, (*b*) $\frac{1}{8}$, (*c*) $\frac{2}{8}$, (*d*) $\frac{3}{8}$, (*b*) $\frac{4}{8}$.

streak is sufficiently weak initially. Nevertheless, the streak instability can lead to the occurrence of coherent quasi-streamwise vortices. In turbulent boundary layers, the width of low-speed streaks, i.e. the half distance between neighbouring low-speed streaks, is typically 50 in wall units and the thickness of near-wall shear layers is roughly half the width or less. This is also the case in the ribbon-induced transition, where near-wall low-speed streaks develop at the later stage of the secondary high-frequency instability (see Nishioka & Asai 1984; Asai & Nishioka 1997). The geometry of these low-speed streaks is not so different from that of the present artificially generated streak. Therefore, if the initial disturbances were sufficiently weak, the instability modes, particularly the symmetric modes might not evolve into discrete vortices before the shear layer undergoes viscous diffusion. In turbu-

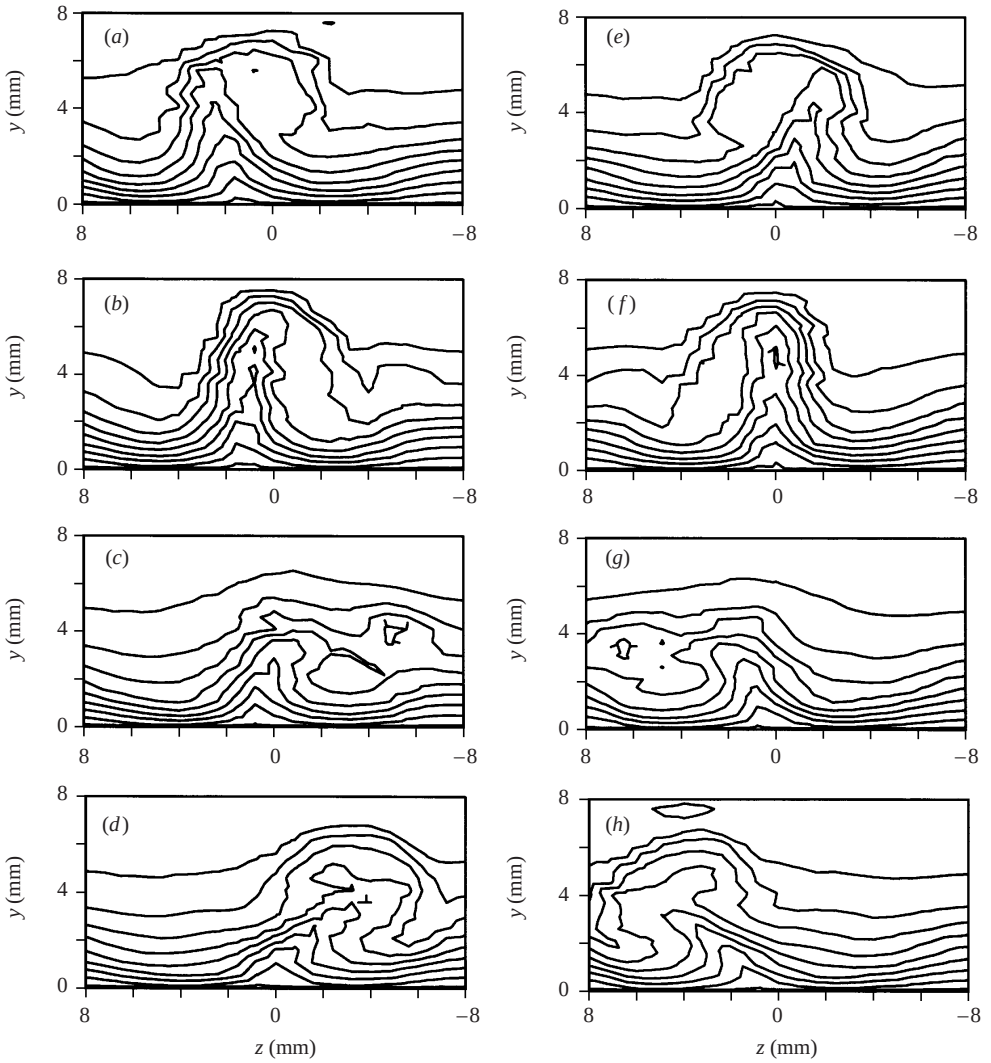

FIGURE 22. Ensemble-averaged velocity field under the excitation of the antisymmetric mode (60 Hz) in the (y,z)-plane at $x - x_0 = 140$ mm in the case of the 7.5 mm wide screen. Time t/T is (*a*) 0, (*b*) $\frac{1}{8}$, (*c*) $\frac{2}{8}$, (*d*) $\frac{3}{8}$, (*e*) $\frac{4}{8}$, (*f*) $\frac{5}{8}$, (*g*) $\frac{6}{8}$, (*h*) $\frac{7}{8}$. Velocity levels range from $0.1U_\infty$ to $0.9U_\infty$.

lent and transitional flows, however, the near-wall flow is highly disturbed, so that the streak instability can be excited by the existing or developing turbulent fluctuations. According to the present linear instability experiment, the streak becomes more unstable to the antisymmetric (sinuous) modes than to the symmetric (varicose) modes when the width of the low-speed streak is narrow and comparable with the shear-layer thickness. So, under strong viscous effects close to the wall, the low-speed streak becomes narrow as mentioned above and might be more stable to symmetric modes. This is consistent with the fact that antisymmetric breakdown of low-speed streaks is dominant in the developed wall turbulence. However, it is important to note that for particular flows, competition between these modes may occur, depending not only on the structure (lateral and vertical dimensions) of low-speed streaks but also on the disturbance environment (or the disturbance condition

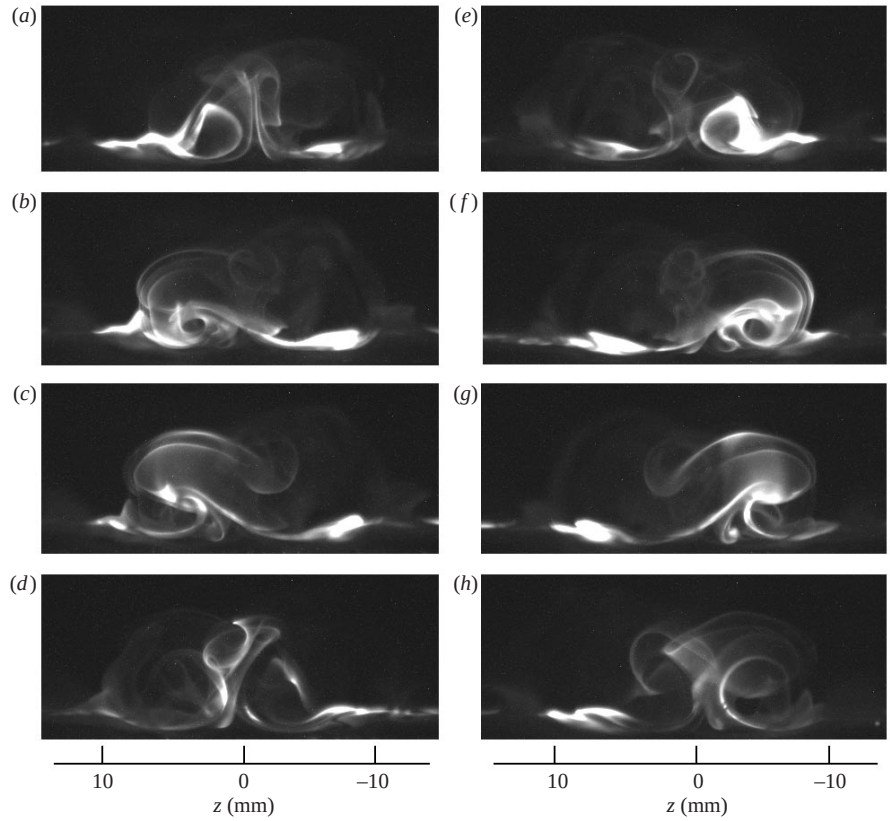

FIGURE 23. Visualization of the development of the antisymmetric mode (60 Hz) in the case of the 7.5 mm wide screen. Cross-sectional view at $x - x_0 = 160$ mm. The time interval between pictures is one-eighth of the forcing period.

triggering the instability), as demonstrated in the present experiment. In fact, it was observed in the ribbon-induced transition experiment cited above that the symmetric breakdown of the low-speed streaks was triggered by hairpin vortices convecting from upstream. Concerning the relative importance of these two modes, further investigations are required including the study of the interaction between the two modes.

Finally, it should be emphasized that in the present experiment, the coherent vortices resulting from the controlled streak instability can be quite periodic. It is found to be very easy to control the development of those vortices. The present experimental configuration is thus very helpful for investigating the dynamics of near-wall coherent vortices as well as for testing various methods of active or passive control of coherent vortices.

The authors wish to express their cordial thanks to Professors S. Iida and H. Sato for their continuous encouragement. This work was in part supported by the Grant-in-Aid for Scientific Research C (no. 10650897) from the Japan Society for the Promotion of Science, the Grant-in-Aid for Scientific Research on Priority Area B (no. 12125203) from the Ministry of Education, Culture, Sports, Science and Technology of Japan, and the Special Research Fund from the Tokyo Metropolitan Government.

REFERENCES

Acarlar, M. S. & Smith, C. R. 1987*a* A study of hairpin vortices in a laminar boundary layer. Part 1. *J. Fluid Mech.* **175**, 1–42.

Acarlar, M. S. & Smith, C. R. 1987*b* A study of hairpin vortices in a laminar boundary layer. Part 2. *J. Fluid Mech.* **175**, 43–83.

Andersson, P., Berggren, M. & Henningson, D. S. 1999 Optimal disturbances and bypass transition in boundary layers. *Phys. Fluids* **11**, 134–150.

Asai, M. & Nishioka, M. 1990 Development of wall turbulence in Blasius flow, in laminar-turbulent transition. In *Laminar–Turbulent Transition* (ed. D. Arnal & R. Michel), pp. 215–222. Springer.

Asai, M. & Nishioka, M. 1995*a* Boundary-layer transition triggered by hairpin eddies at subcritical Reynolds numbers. *J. Fluid Mech.* **297**, 101–122.

Asai, M. & Nishioka, M. 1995*b* Subcritical disturbance growth caused by hairpin eddies. In *Laminar–Turbulent Transition* (ed. R. Kobayashi), pp. 111–118. Springer.

Asai, M. & Nishioka, M. 1997 Development of wall turbulence structure in transitional flows. In *Theoretical and Applied Mechanics 1996* (ed. R. Tatsumi, T. Kambe & E. Watanabe), pp. 121–138. Elsevier.

Asai, M., Sawada, K. & Nishioka, M. 1996 Development of turbulent patch in a subcritical boundary layer. *Fluid Dyn. Res.* **18**, 1151–1168.

Bakchinov, A. A., Westin, K. J. A., Kozlov, V. V. & Alfredsson, P. H. 1998 Experiments on localized disturbances in a flat plate boundary layer. Part 1. Interaction between localized disturbances and T-S waves. *Eur. J. Mech.* B/Fluids **17**, 847–873.

Carlson, D. R., Widnall, S. E. & Peeters, M. F. 1982 A flow-visualization study of transition in plane Poiseuille flow. *J. Fluid Mech.* **121**, 487–505.

Doligalski, T. L., Smith, C. R. & Walker, J. D. A. 1994 Vortex interactions with walls. *Annu. Rev. Fluid Mech.* **26**, 573–616.

Elofsson, P. A., Kawakami, M. & Alfredsson, P. H. 1999 Experiments on the stability of streamwise streaks in plane Poiseuille flow. *Phys. Fluids* **11**, 915–930.

Haidari, A. H. & Smith, C. R. 1994 The generation and regeneration of single hairpin vortices. *J. Fluid Mech.* **277**, 135–162.

Hall, P. & Horseman, N. J. 1991 The linear inviscid secondary instability of longitudinal vortex structures in boundary layers. *J. Fluid Mech.* **232**, 357–375.

Hamilton, J. M., Kim, J. & Waleffe, F. 1995 Regeneration mechanisms of near-wall turbulence structures. *J. Fluid Mech.* **287**, 317–348.

Hultgren, L. S. & Gustavsson, L. H. 1981 Algebraic growth of disturbances in a laminar boundary layer. *Phys. Fluids* **24**, 1000–1004.

Itano, T. & Toh, S. 2001 The dynamics of bursting process in wall turbulence. *J. Phys. Soc. Japan* **70**, 703–716.

Jeong, J. & Hussain, F. 1995 On the identification of a vortex. *J. Fluid Mech.* **285**, 69–94.

Jeong, J., Hussain, F., Schoppa, W. & Kim, J. 1997 Coherent structures near the wall in a turbulent channel flow. *J. Fluid Mech.* **332**, 185–214.

Jimenez, J. & Moin, P. 1991 The minimal flow unit in near-wall turbulence. *J. Fluid Mech.* **225**, 213–240.

Johansson, A.V., Alfredsson, P. H. & Kim, J. 1991 Evolution and dynamics of shear-layer structures in near-wall turbulence. *J. Fluid Mech.* **224**, 579–599.

Kim, J., Moin, P. & Moser, R. D. 1987 Turbulence statistics in fully developed channel flow at low Reynolds number. *J. Fluid Mech.* **177**, 133–166.

Kline, S. J., Reynolds, W. C., Schraub, F. A. & Runstadler, P. W. 1997 The structure of turbulent boundary layers. *J. Fluid Mech.* **30**, 741–773.

Landahl, M. T. 1980 A note on an algebraic instability of inviscid parallel shear flows. *J. Fluid Mech.* **98**, 243–251.

Luchini, P. 2000 Reynolds-number-independent instability of the boundary layer over a flat surface: optimal perturbations. *J. Fluid Mech.* **404**, 289–309.

Matsubara, M., Bakchinov, A. A., Fransson, J. H. M. & Alfredsson, P. H. 2000 Growth and breakdown of streaky structures in boundary-layer transition induced by freestream turbulence. In *Laminar–Turbulent Transition* (ed. H. Fasel & W. Saric), pp. 371–376. Springer.

Matsui, T. 1980 Visualization of turbulent spots in the boundary layer along a flat plate in water flow. In *Laminar–Turbulent Transition* (ed. R. Eppler & H. Fasel), pp. 288–296. Springer.

Mochizuki, M. 1961 Smoke observation on boundary layer transition caused by a spherical roughness element. *J. Phys. Soc. Japan* **16**, 995–1008.

Morkovin, M. V. & Reshotko, E. 1990 Dialogue on progress and issues in instability and transition research. In *Laminar–Turbulent Transition* (ed. D. Arnal & R. Michel), pp. 3–39. Springer.

Nishioka, M. & Asai, M. 1984 Evolution of Tollmien–Schlichting waves into wall turbulence. In *Turbulence and Chaotic Phenomena in Fluids* (ed. T. Tatsumi), pp. 87–92. North-Holland.

Nishioka, M., Asai, M. & Furumoto, S. 1994 Critical conditions for wall turbulence generation. In *Fluid- and Gasdynamics* (ed. G. H. Schnerr, R. Bohning, K. Buhler & W. Frank). Acta Mechanica, suppl. 4, pp. 87–94. Springer.

Nishioka, M., Asai, M. & Iida, S. 1980 Experimental investigation of the secondary instability. In *Laminar–Turbulent Transition* (ed. R. Eppler & H. Fasel), pp. 37–46. Springer.

Nishioka, M., Asai, M. & Iida, S. 1981 Wall phenomena in the final stage of transition to turbulence. In *Laminar–Turbulent Transition* (ed. R. Eppler & H. Fasel), pp. 113–126. Springer.

Nishioka, M., Iida, S. & Ichikawa, Y. 1975 An experimental investigation of the stability of plane Poiseuille flow. *J. Fluid Mech.* **72**, 731–751.

Park, D. S. & Huerre, P. 1994 Primary and secondary instabilities of the asymptotic suction boundary layer on a curved plate. *J. Fluid Mech.* **283**, 249–272.

Peridier, V. J., Smith, F. T. & Walker, J. D. A. 1991*a* Vortex-induced boundary-layer separation. Part 1. The unsteady limit problem $Re \rightarrow \infty$. *J. Fluid Mech.* **232**, 99–131.

Peridier, V. J., Smith, F. T. & Walker, J. D. A. 1991*b* Vortex-induced boundary-layer separation. Part 2. The unsteady interacting boundary-layer theory. *J. Fluid Mech.* **232**, 133–165.

Perry, A. E., Lim, T. T. & Teh, E. W. 1981 A visual study of turbulent spots. *J. Fluid Mech.* **104**, 387–405.

Rist, U. & Fasel, H. 1995 Direct numerical simulation of controlled transition in a flat-plate boundary layer. *J. Fluid Mech.* **298**, 211–248.

Robinson, S. K. 1991 Coherent motions in the turbulent boundary layer. *Annu. Rev. Fluid Mech.* **23**, 601–639.

Sandham, N. D. and Kleiser, L. 1992 The late stages of transition to turbulence in channel flow. *J. Fluid Mech.* **245**, 319–348.

Saric, W. S. 1994 Görtler vortices. *Annu. Rev. Fluid Mech.* **26**, 379–409.

Schoppa, W. & Hussain, F. 1997 Genesis and dynamics of coherent structures in near-wall turbulence: a new look. In *Self-Sustaining Mechanisms of Wall Turbulence* (ed. R. L. Panton), Chap. 16, pp. 385–422. Computational Mechanics Publications.

Schoppa, W. & Hussain, F. 2000 Coherent structure dynamics in near-wall turbulence. *Fluid Dyn. Res.* **26**, 119–139.

Singer, B. A. & Joslin, R. D. 1994 Metamorphosis of a hairpin vortex into young turbulent spot. *Phys. Fluids* **6**, 3724–3730.

Smith, C. R., Walker, J. D. A., Haidari, A. H. & Sobrun, U. 1991 On the dynamics of near-wall turbulence. *Phil. Trans. R. Soc. Lond.* A **336**, 131–175.

Swearingen, J. D. & Blackwelder, R. F. 1987 The growth and breakdown of streamwise vortices in the presence of a wall. *J. Fluid Mech.* **182**, 255–290.

Van Dommelen, L. L. & Cowley, S. J. 1990 On the Lagrangian description of unsteady boundary-layer separation. Part 1. General theory. *J. Fluid Mech.* **210**, 627–645.

Westin, K. J. A., Bakchinov, A. A., Kozlov, V. V. & Alfredsson, P. H. 1998 Experiments on localized disturbances in a flat plate boundary layer. Part 1. The receptivity and evolution of a localized free stream disturbance. *Eur. J. Mech.* B/Fluids **17**, 823–846.

Yu, X. & Liu, J. T. C. 1991 On the secondary instability in Görtler flow. *Phys. Fluids* A **3**, 1845–1847.

Zhou, J, Adrian, R. J., Balachandar, S. & Kendall, T. M. 1999 Mechanisms for generating coherent packets of hairpin vortices in channel flow. *J. Fluid Mech.* **387**, 353–396.